



Cite this: DOI: 10.1039/c8nj04524k

A γ -Fe₂O₃-modified nanoflower-MnO₂/attapulgite catalyst for low temperature SCR of NO_x with NH₃

 Aijuan Xie,^{†a} Yiyang Tao,^{†b} Xiang Jin,^a Pengfei Gu,^a Xiaoyan Huang,^a
Xingmeng Zhou,^a Shiping Luo,^{ib} *^a Chao Yao^a and Xiazhang Li^{ib} ^a

A mesoporous γ -Fe₂O₃-modified nanoflower-MnO₂/attapulgite (γ -Fe₂O₃/nf-MnO₂-ATP) catalyst was fabricated through a facile hydrothermal method. The results of TEM and XRD indicated that γ -Fe₂O₃/nf-MnO₂-ATP presented a beautiful nanoflower shape and good dispersion. The BET results showed that the specific surface area and pore volume of γ -Fe₂O₃/nf-MnO₂-ATP significantly increased after surface modification with γ -Fe₂O₃. Also, the XPS and NH₃-TPD results illustrated that the γ -Fe₂O₃ coating could enhance the amounts of surface chemisorbed oxygen and acidic sites. SO₂ and H₂O tolerance tests and stability tests demonstrated that γ -Fe₂O₃/nf-MnO₂-ATP can effectively inhibit SO₂ and H₂O poisoning and improve the stability of the catalyst. The superior SCR performance can be attributed to the abundant acid sites, the strong adsorption of NO_x, and the formation of more oxygen vacancies as well as metal-metal interactions. Therefore, γ -Fe₂O₃/nf-MnO₂-ATP was proved to be an excellent catalyst for NH₃-SCR and may be of interest in other environmental catalysis applications.

Received 6th September 2018,
Accepted 30th December 2018

DOI: 10.1039/c8nj04524k

rsc.li/njc

Introduction

Over the past few decades, nitrogen oxide (NO_x) emissions have increased with the increases in energy consumption and in the number of cars each year. It is generally considered that NO_x is the major cause of acid rain, haze, photochemical smog, ozone depletion and greenhouse effects; it has gradually become one of the largest sources of environmental pollution.¹ Therefore, it is very important to research and develop efficient, stable and inexpensive denitration catalysts which can transform the NO_x emitted from coal-fired power plants and motor vehicles into non-toxic N₂.² Selective catalytic reduction of NO_x with NH₃ (NH₃-SCR) was the first denitration technology to be developed and used in the 1960s in Japan. The main principle of SCR is that NH₃ or urea, as a reductant, reacts selectively with NO to generate non-toxic N₂ at low temperature under the action of a metal catalyst. Due to its high efficiency of denitration, this process has become the mainstream flue gas denitration technology at home and abroad. Catalysts used in the current SCR denitration technology mainly employ V₂O₅-WO₃ as the main active components and TiO₂ as the carrier. These catalysts have high denitration efficiency, high stability, and superior sulfur (SO₂)

resistance performance; therefore, they have become the mainstream in the field of flue gas denitration catalysts.³ However, with the development of denitration technology and environmental protection requirements, the defects of traditional V₂O₅-WO₃/TiO₂ catalysts became increasingly obvious, such as higher reaction temperature (300–450 °C), toxic vanadium species and the high cost of WO₃. The present stage of denitration technology in general is to install desulphurization and dust removal devices before the denitration section in order to avoid decreased activity of the denitration catalyst caused by particles in flue gas and SO₂, which can cause the temperature of the flue gas in the denitration phase to decrease to 100–300 °C. The denitration efficiency of traditional V₂O₅-WO₃/TiO₂ catalysts is low in this temperature range; thus, it cannot meet the requirements of the present stage of denitration.⁴ Meanwhile, the mechanical properties and molding performance of traditional V₂O₅-WO₃/TiO₂ catalysts are poor; the material is mainly coated on cordierite, stainless steel plate, or a manufactured homogeneous extruded honeycomb catalyst which consists of titanium oxide, tungsten oxide, vanadium pentoxide and glass fiber with polyvinyl alcohol as the binder in practical applications.⁵ Therefore, the research and development of low temperature denitration catalysts with excellent denitration performance between 100 °C and 300 °C to replace traditional V₂O₅-WO₃/TiO₂ catalysts has become a current research focus.

In recent years, Mn-based catalysts as the main active component have been widely applied in this field; they exhibit excellent denitration performance at low temperature (100–300 °C) due to their strong oxidation ability and ammonia activation.⁶

^a School of Petrochemical Engineering, Changzhou University, Changzhou 213164, P. R. China. E-mail: shiping_luo@163.com; Fax: +86 519 86330158; Tel: +86 519 86330158

^b School of Fine Arts, Nanjing Normal University, Nanjing, 210046, P. R. China

[†] Both are equal contribution to this work and should be regarded as first joint authors.

However, single Mn-based catalysts suffer from the disadvantages of lower N_2 selectivity and lower SO_2 resistance.⁷ Therefore, in order to address the defects of single Mn-based catalysts, many researchers have chosen Fe,^{8,9} Ce,^{10,11} Cr,¹² Ti¹³ and other metal oxides as catalytic components to dope MnO_x to obtain excellent denitration performance. Fe_2O_3 has recently been widely studied as a primary catalyst due to its low toxicity, high thermal stability¹⁴ and excellent anti- SO_2 performance. France *et al.*¹⁵ used manganese acetate and ferric nitrate as precursors to form a sol and then obtained $FeMnO_x$ catalysts by drying and roasting. Their test results showed that the addition of Fe greatly enhanced the activity and SO_2 resistance of the catalysts; over 90% NO_x conversion could be achieved at the low temperature of 150 °C, and the SO_2 and H_2O resistance of $FeMnO_x$ catalysts are also superior. Furthermore, Liu *et al.*¹⁶ prepared α - Fe_2O_3 and γ - Fe_2O_3 , respectively, through calcining at different temperatures and compared the denitration performance of α - Fe_2O_3 and γ - Fe_2O_3 under the same conditions. It was found that NH_3 and NO were more easily adsorbed on the surface of γ - Fe_2O_3 relative to α - Fe_2O_3 ; also, γ - Fe_2O_3 showed superior denitration performance, N_2 selectivity, and NO_x conversion rates.

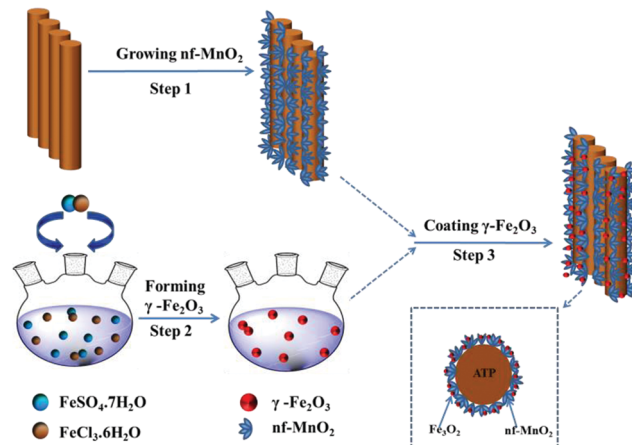
Carrier-type catalysts are conducive to dispersion of active components; many reports have been published on different carriers, such as Cu-SAPO-34¹⁷ and meso- TiO_2 .¹⁸ Attapulgite (ATP) is a clay mineral that is rich in magnesium aluminosilicate and shows good plasticity. ATP is beneficial as a catalyst carrier for catalyst formation. Also, its rich channels are advantageous to gas adsorption, thus improving the performance of catalysts. Therefore, ATP is also widely used in the catalytic field.^{19,20}

Therefore, in this work, ATP was first purified to remove as many surface impurities as possible. Then, the purified ATP as a carrier was mixed with $KMnO_4$ solution; the pH value was adjusted to ~ 3 with acetic acid. $KMnO_4$ was slowly decomposed to form flaky MnO_2 tightly coated on the surface of the ATP under low temperature hydrothermal conditions to synthesize nanoflower- MnO_2 -ATP (nf- MnO_2 -ATP). After that, the high-performance γ - Fe_2O_3 nanoparticles were used to modify the surface of nf- MnO_2 -ATP under low temperature hydrothermal conditions to prepare the γ - Fe_2O_3 /nf- MnO_2 -ATP denitration catalyst. The preparation conditions of the γ - Fe_2O_3 /nf- MnO_2 -ATP catalyst were gentle, simple and feasible. The as-prepared catalyst exhibited excellent NH_3 -SCR denitration performance at low temperature. The enhanced N_2 selectivity and SO_2 resistance are due to the excellent anti- SO_2 performance derived from γ - Fe_2O_3 and the unique nanoflower morphology of γ - Fe_2O_3 /nf- MnO_2 -ATP.

Experimental

Catalyst preparation

Preparation of nf- MnO_2 -ATP. ATP raw material was provided by Nanda Zijin Technology Group Co, Ltd (Changzhou, China); other chemicals were of analytical grade and were supplied by Sinopharm Chemical Reagent Co., Ltd (Shanghai, China). The ATP raw material was pretreated with mixed acid (volume ratio of H_2SO_4/HNO_3 was 3:1) to remove surface impurities and



Scheme 1 Schematic of the synthesis of γ - Fe_2O_3 /nf- MnO_2 -ATP.

introduce $-OH$ onto its surface. First, the acid-treated ATP was dispersed in deionized water to form a dispersed slurry under ultrasonic treatment; 2.0 g of $KMnO_4$ was dissolved in the ATP suspension, and the mixed liquor was subjected to continued ultrasonic processing for 20 min to thoroughly mix the ATP with $KMnO_4$. Then, the mixture was transferred into a 500 mL three-necked flask, and 40 mL of glacial acetic acid was added to it to adjust the pH value of the solution to ~ 3 ; the temperature of the solution was maintained at 78 °C during the reaction for 4 h, followed by filtering and washing to neutral. The resulting filter cake was dried at 80 °C to obtain nf- MnO_2 -ATP.

0.15 g of $FeSO_4 \cdot 7H_2O$ and 0.29 g of $FeCl_3 \cdot 7H_2O$ were dissolved in deionized water and then moved into a three-necked flask to conduct a reflux reaction at 90 °C; air bubbles were injected with an air pump during the progress of the reaction. After reacting for 2 h, the resulting liquid was cooled to room temperature; then, the pH value was adjusted with ammonia water to about 10, and the mixture continued to react for 5 h under water bath reflux conditions to age the sedimentary grains. Next, the nf- MnO_2 -ATP suspension was slowly added, and this system was maintained with stirring at room temperature for 1 h so that the γ - Fe_2O_3 nanoparticles were gradually adsorbed onto the surface of nf- MnO_2 -ATP by charge effects; thus, γ - Fe_2O_3 /nf- MnO_2 -ATP was acquired. The whole preparation process of γ - Fe_2O_3 /nf- MnO_2 -ATP is illustrated in Scheme 1.

Catalyst characterization

X-ray diffraction (XRD) analyses of the powered samples were performed using an X-ray diffractometer with a Cu anode (D/Max 2500 PC, Rigaku Corporation, Japan) running at 60 kV and 30 mA with a scan range from 10° to 80° at 3° min^{-1} . The transmission electron microscopic (TEM) images were obtained using a JEM-2100 electron microscope (JEOL, Japan) with an accelerating voltage of 200 kV. The zeta potential values were determined with a nano-laser particle size and zeta potential analyzer (ZEN 3600, Malvern, UK). The specific surface areas were determined by the isothermal N_2 adsorption/desorption method at 77 K using a Micromeritics Adsorption instrument

and were then calculated from the adsorbed nitrogen volumes by an automatic volumetric apparatus according to standard Brunauer–Emmett–Teller (BET) theory. The X-ray photoelectron spectroscopy (XPS) data were obtained with an Escalab 250Xi electron spectrometer from Thermo Fisher Scientific using Al K α radiation. The binding energy was corrected using the C 1s spectrum at 284.8 eV.

Both the temperature-programmed desorption of NH₃ (NH₃-TPD) and the temperature-programmed reduction of H₂ (H₂-TPR) were conducted using a TP 5080 auto-adsorption apparatus (XQ, Tianjin). About 100 mg of sample was pretreated at 250 °C for 30 min using high purity He (35 mL min⁻¹); then, adsorption under NH₃ or H₂/N₂ (the mole fraction of H₂ was 10%) was carried out over the catalyst. Finally, the sample was heated from ambient temperature to 800 °C in N₂ atmosphere at a rate of 10 °C min⁻¹. The desorption signal of the sample was recorded with the relevant detector.

SCR performance tests

SCR activity measurements of the catalyst were performed in a fixed bed quartz reactor (i.d. 15 mm) supplied by Huasi Instrument Co., Ltd (Hunan, China). The reaction was carried out with a 2 L min⁻¹ total flow rate (under ambient conditions) of a mixture of 1000 ppm NO, 1000 ppm NH₃, 3 vol% O₂, 200 ppm SO₂ (when used), 10% H₂O (when used) and N₂ as the balance gas in the inlet with a gas hourly space velocity (GHSV) of ca. 45 000 h⁻¹. Before testing, mixed gas (NO + NH₃ + N₂ + O₂) was continually aerated into the fixed bed quartz reactor for 30 min to saturate the catalyst and thus avoid a concentration decrease of NO_x arising from adsorption of the catalyst. 3 mL of catalyst were used for each SCR activity test, and water vapor was dosed *via* saturator. The inlet and outlet concentrations of NO_x were continually measured by an NO/NO₂/NO_x analyzer (KM9106, Kane International Ltd). All the data were obtained after 30 min as the SCR reaction reached the steady state. NO_x conversion and N₂ selectivity were respectively calculated using the expressions

$$\text{NO}_x \text{ conversion (\%)} = \frac{[\text{NO}_x]_{\text{in}} - [\text{NO}_x]_{\text{out}}}{[\text{NO}_x]_{\text{in}}} \times 100\%. \quad (1)$$

$$\text{N}_2 \text{ selectivity (\%)} = \frac{[\text{NO}]_{\text{in}} + [\text{NH}_3]_{\text{in}} - [\text{NO}_2]_{\text{out}} - 2[\text{N}_2\text{O}]}{[\text{NO}]_{\text{in}} + [\text{NH}_3]_{\text{in}}} \times 100\% \quad (2)$$

where [NO_x]_{in} and [NO_x]_{out} represent the inlet and outlet concentrations of NO_x in the steady-state status, respectively.

Results and discussion

Characterization analysis

XRD patterns. The crystal structures of ATP, γ -Fe₂O₃, nf-MnO₂-ATP, and γ -Fe₂O₃/nf-MnO₂-ATP were analyzed by XRD, and the results are presented in Fig. 1. The XRD pattern of γ -Fe₂O₃ exhibits characteristic peaks at $2\theta = 30.2^\circ$, 35.6° , 43.2° , 53.7° , 57.2° , and 62.9° , which are assigned to the (220), (311), (400), (422), (511) and (400) planes of γ -Fe₂O₃,

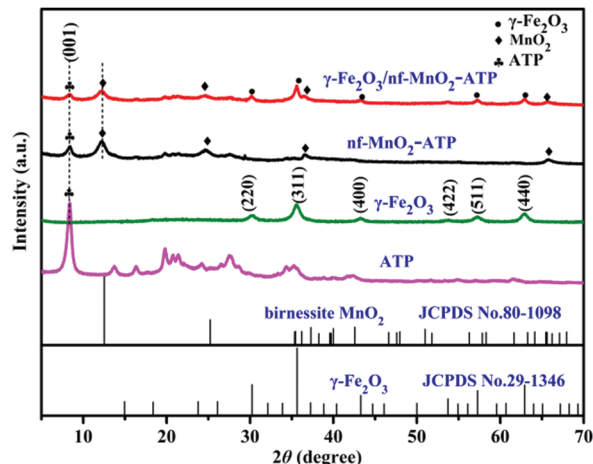


Fig. 1 XRD patterns of the different catalysts.

respectively (JCPDS No. 39-1346). This proves that the Fe₂O₃ prepared by the low temperature hydrothermal method mainly exists in the form of γ -Fe₂O₃.²¹ For nf-MnO₂-ATP, four broad peaks at 12.5° , 25.2° , 37.3° and 65.4° belonging to birnessite MnO₂ (δ -MnO₂) (JCPDS No. 80-1098) can be observed,²² while the strong peak at $2\theta = 8.42^\circ$ derived from ATP significantly weakened. The main reason for this is that KMnO₄ is decomposed into MnO₂, which is adsorbed by the ATP and coated on its surface under acidic conditions, resulting in a decrease of the strength of the ATP diffraction peak.²³ For γ -Fe₂O₃/nf-MnO₂-ATP, a set of peaks at $2\theta = 30.2^\circ$, 35.6° , 43.2° , 53.7° , 57.2° , and 62.9° can still be clearly observed, which is in good agreement with the characteristic diffraction peaks of pure γ -Fe₂O₃. Also, the strong peaks at around $2\theta = 8.42^\circ$ and 12.5° and other weak peaks arising from ATP and δ -MnO₂ are retained; however, they become thin relative to those of ATP and nf-MnO₂-ATP due to their interactions with each other, indicating that γ -Fe₂O₃ nanoparticles have been successfully loaded on the surface of nf-MnO₂-ATP.

TEM images

The micro-morphologies of the different samples were observed by TEM at different magnifications, and the results are displayed in Fig. 2. Fig. 2a shows the typical rod-shaped ATP morphology with a diameter of 20 to 30 nm. Fig. 2b presents beautiful MnO₂ nanoflowers, which are uniformly coated on the ATP surface and combined closely with the ATP. The coating thickness is in the range of 30 to 60 nm after the MnO₂ nano-flower coating. Moreover, after acidification treatment, ATP presents good dispersibility; the main reason for this may be that acidification can remove impurities on the surface of ATP, decrease the aggregation of ATP bundles, and introduce oxygen-containing functional groups on the surface, which is beneficial to the dispersion and deposition of MnO₂.²⁴ The nano-flower-shaped MnO₂ produced by the hydrothermal method has a larger gas contact area, which is more favorable to the adsorption of NH₃ and NO on the surface of the catalyst than the nano-particle MnO₂ prepared by a conventional precipitation method. Fig. 2c shows γ -Fe₂O₃ nanoparticles

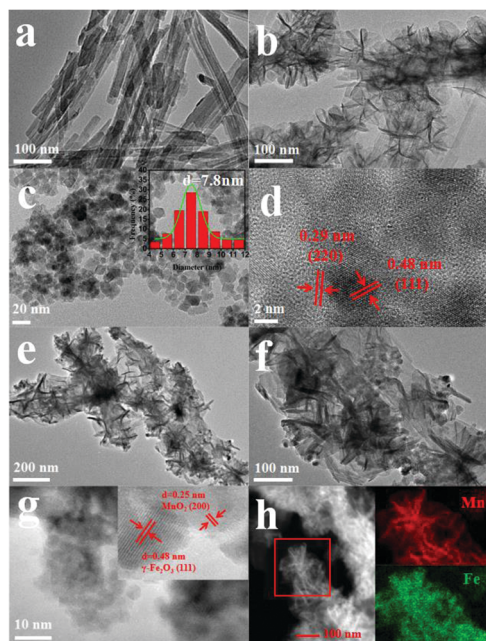


Fig. 2 TEM images of ATP (a), $\text{nf-MnO}_2\text{-ATP}$ (b), $\gamma\text{-Fe}_2\text{O}_3$ (c, d, inset in c: statistical analysis of particle size distribution), and $\gamma\text{-Fe}_2\text{O}_3/\text{nf-MnO}_2\text{-ATP}$ (e and f); HRTEM images (g) and EDX-mapping (h) of $\gamma\text{-Fe}_2\text{O}_3/\text{nf-MnO}_2\text{-ATP}$.

prepared through the low temperature hydrothermal method. As can be seen, $\gamma\text{-Fe}_2\text{O}_3$ presents a slight aggregation phenomenon; the dominant reason for this is that $\gamma\text{-Fe}_2\text{O}_3$ itself is a ferromagnetic material and thus can readily undergo aggregation due to magnetic attraction between particles. Moreover, $\gamma\text{-Fe}_2\text{O}_3$ presents nanoparticle distribution; the large surface energy between the nanoparticles can readily cause agglomeration of the particles.²⁵ The average particle size of $\gamma\text{-Fe}_2\text{O}_3$ is about 7.8 nm (inset of Fig. 2c). Fig. 2d shows a high resolution transmission electron microscopy (HRTEM) image of $\gamma\text{-Fe}_2\text{O}_3$; the lattice fringe distribution of $\gamma\text{-Fe}_2\text{O}_3$ can be seen clearly from the picture, and the widths of the grid lines are 0.29 and 0.48 nm, respectively, corresponding to the (220) and (111) crystal planes of $\gamma\text{-Fe}_2\text{O}_3$.²⁶ Fig. 2e and 2f show TEM images of $\gamma\text{-Fe}_2\text{O}_3/\text{nf-MnO}_2\text{-ATP}$. It can be seen from Fig. 2e that after surface modification with $\gamma\text{-Fe}_2\text{O}_3$, the flower-like surface morphology of $\text{nf-MnO}_2\text{-ATP}$ shows almost no change. MnO_2 with a nanometer morphology is still coated on the surface of the ATP; however, tiny particles with a uniform distribution appear in the outer surface of the $\text{nf-MnO}_2\text{-ATP}$, which can be clearly observed from Fig. 2f, where the particles have been successfully embedded in the $\text{nf-MnO}_2\text{-ATP}$ flake petals. This is beneficial to uniform dispersion of $\gamma\text{-Fe}_2\text{O}_3$ and, thus, avoiding catalyst aggregation in practical applications under high temperature conditions. Fig. 2g shows HRTEM images of $\gamma\text{-Fe}_2\text{O}_3/\text{nf-MnO}_2\text{-ATP}$.

It can be found that two different lattice fringes appear on the surface of $\gamma\text{-Fe}_2\text{O}_3/\text{nf-MnO}_2\text{-ATP}$; the lattice fringe spacings are 0.48 nm and 0.25 nm, respectively, which belong to the (111) crystal plane of $\gamma\text{-Fe}_2\text{O}_3$ and the (200) crystal plane of $\delta\text{-MnO}_2$, respectively, according to a literature report.²⁷

Table 1 Zeta potentials of $\gamma\text{-Fe}_2\text{O}_3$ and $\text{nf-MnO}_2\text{-ATP}$

pH value	Zeta potential (mV)	
	$\gamma\text{-Fe}_2\text{O}_3$	$\text{nf-MnO}_2\text{-ATP}$
1	17.5	1.07
3	20.2	-4.62
5	23.2	-5.98
7	33.3	-18.3
9	-29.3	-32.4

Fig. 2h presents EDX-mapping images for $\gamma\text{-Fe}_2\text{O}_3/\text{nf-MnO}_2\text{-ATP}$. Mn element is present in the nano-flowers coated on the external surface of the ATP, while Fe element, which shows graininess, is adsorbed on the surface of $\text{nf-MnO}_2\text{-ATP}$. Therefore, it is proved that the active component of the catalyst in the as-assembled $\gamma\text{-Fe}_2\text{O}_3/\text{nf-MnO}_2\text{-ATP}$ has good dispersion, which is conducive to improvement of the catalyst activity in $\text{NH}_3\text{-SCR}$ denitration.

In addition, in order to further verify whether $\gamma\text{-Fe}_2\text{O}_3$ particles were successfully loaded on the surface of $\text{nf-MnO}_2\text{-ATP}$, the zeta potentials of the as-prepared $\gamma\text{-Fe}_2\text{O}_3$ and $\text{nf-MnO}_2\text{-ATP}$ were investigated to test the surface charges under different pH values. The pH value of each solution was adjusted with acetic acid or ammonia, and the test data are shown in Table 1. It can be seen from Table 1 that the zeta potentials of $\gamma\text{-Fe}_2\text{O}_3$ (33.3 mV) and $\text{nf-MnO}_2\text{-ATP}$ (-18.3 mV) have diametrically opposite charges at pH 7, which can generate attractive charges between them; thus, $\gamma\text{-Fe}_2\text{O}_3$ can be successfully adsorbed on the surface of $\text{nf-MnO}_2\text{-ATP}$. Compared to mechanical mixing, the charge attraction between components can strengthen the combination of $\gamma\text{-Fe}_2\text{O}_3$ and $\text{nf-MnO}_2\text{-ATP}$, thus decreasing aggregation and shedding of particles in the test process.²⁸ Hence, in view of the XRD and TEM results, we can further deduce that $\gamma\text{-Fe}_2\text{O}_3/\text{nf-MnO}_2\text{-ATP}$ has been successfully fabricated.

BET analysis

The N_2 adsorption-desorption isotherms of ATP, $\text{nf-MnO}_2\text{-ATP}$ and $\gamma\text{-Fe}_2\text{O}_3/\text{nf-MnO}_2\text{-ATP}$ and the corresponding pore size distributions are displayed in Fig. 3. It can be seen that all the materials have similar adsorption curves and obvious hysteresis loops in the P/P_0 range of 0.5 to 1.0. According to the IUPAC classification, both samples show typical type II adsorption isotherms with type H_3 hysteresis loops, suggesting the existence of well-defined mesoporous structures on the surfaces of the two catalysts.²⁹ Meanwhile, on the basis of the BJH (Barret-Joyner-Halenda) model, the pore size distributions of the samples were also calculated, and the results are shown in Fig. 3b; all the materials show two different pore size distributions within 2 to 30 nm. The distribution around 3.8 nm mainly arises from the surface adsorption holes of the ATP clay, and the distribution around 21.2 nm arises primarily from staggered stacking of ATP. After nf-MnO_2 surface loading, the pore size distribution of $\text{nf-MnO}_2\text{-ATP}$ is weakened around 21 nm, while there is a significant increase at 3.88 nm. This may be due to the covering of flaky MnO_2 on the ATP surface, which divides some larger pores into smaller ones.³⁰

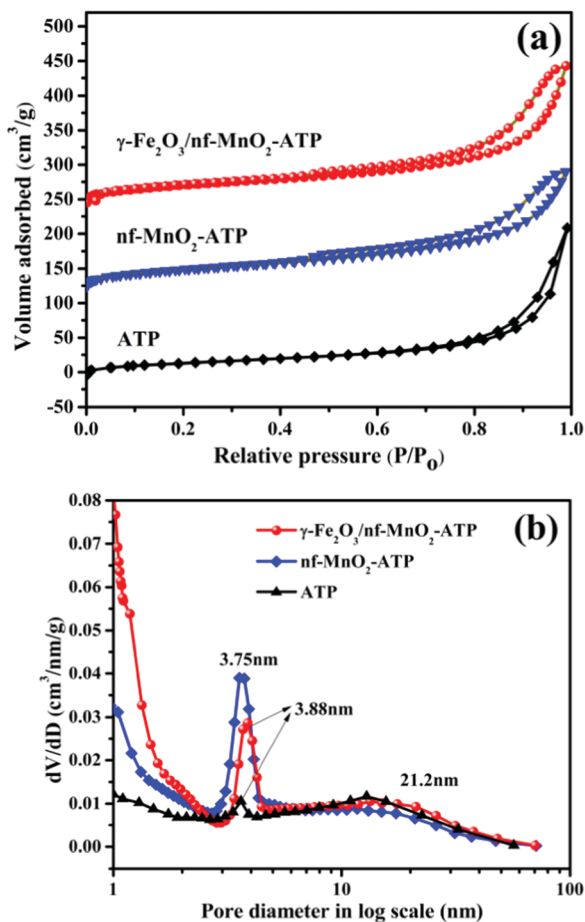


Fig. 3 N_2 adsorption–desorption isotherms (a) and corresponding pore size distributions of ATP, $nf-MnO_2-ATP$ and $\gamma-Fe_2O_3/nf-MnO_2-ATP$ (b).

Furthermore, after surface modification by $\gamma-Fe_2O_3$, the number of adsorption holes in the range of 3.7 to 3.9 nm decreased slightly; this may be because $\gamma-Fe_2O_3$ loading covered some of the holes on the surface of the ATP.

Furthermore, to better reveal the porous structures of the as-prepared catalysts, their specific surface areas, pore volumes and pore diameters are listed in Table 2. Both catalysts show larger specific surface areas due to the structural advantages of ATP itself, which can not only provide a larger specific surface area and porous structures, but can also be helpful for gas adsorption and contact reactions. Additionally, the plasticity of ATP itself is beneficial to the catalyst molding.³¹ Compared with $nf-MnO_2-ATP$, the specific surface area and pore volume of $\gamma-Fe_2O_3/nf-MnO_2-ATP$ show significant increases, and the pore size also shows a certain increase. It is generally recognized that

Table 2 Specific surface areas, pore volumes and pore sizes of $nf-MnO_2-ATP$ and $\gamma-Fe_2O_3/nf-MnO_2-ATP$

Catalyst	Specific surface area ($m^2 g^{-1}$)	Pore volume ($cm^3 g^{-1}$)	Pore diameter (nm)
$nf-MnO_2-ATP$	166.0	0.294	7.09
$\gamma-Fe_2O_3/nf-MnO_2-ATP$	199.7	0.359	7.29

a larger specific surface area and pore volume are advantageous to adsorption and contact of gas on a surface; these can provide more reaction sites for catalytic reactions, which can improve the NO_x conversion rate of the catalyst.³²

XPS analysis

XPS was employed to characterize the near surface atomic compositions and the chemical states of $nf-MnO_2-ATP$ and $\gamma-Fe_2O_3/nf-MnO_2-ATP$. The wide survey spectra of $nf-MnO_2-ATP$ and $\gamma-Fe_2O_3/nf-MnO_2-ATP$ reveal the presence of Mn, Fe, and O elements,³³ and the results are displayed in Fig. 4(a). It can be seen that only Mn 2p and O 1s peaks are present in the survey spectrum of $nf-MnO_2-ATP$; meanwhile, after modification by $\gamma-Fe_2O_3$, the Fe 2p peak at a binding energy near 710 eV appears in the survey spectrum of $\gamma-Fe_2O_3/nf-MnO_2-ATP$, indicating that $\gamma-Fe_2O_3$ was successfully combined with $nf-MnO_2-ATP$.

Fig. 4b shows the Mn 2p spectra, where the two main peaks of Mn 2p_{3/2} and Mn 2p_{1/2} can be observed at 641.9 eV and 653.9 eV, respectively. The Mn 2p_{3/2} spectra can be deconvoluted into two peaks that appear at 642.1 eV and 643.5 eV, corresponding to Mn³⁺ (641.6 to 642.3 eV) and Mn⁴⁺ (642.3 to 644.5 eV), respectively.³³

Table 3 displays the surface elements of the catalysts; the percentages of Mn⁴⁺/(Mn⁴⁺ + Mn³⁺) are 36.9% for $nf-MnO_2-ATP$ and 39.5% for $\gamma-Fe_2O_3/nf-MnO_2-ATP$, implying that the Mn⁴⁺ content in $nf-MnO_2-ATP$ increases after modification with $\gamma-Fe_2O_3$. The increase of Mn⁴⁺ content with a higher oxidation state is helpful for redox reactions and can enhance the conversion from NO to NO₂; more NO₂ is conducive to fast SCR reactions and also improves the activation of the catalyst during low temperature SCR.³⁴

In Fig. 4c, two distinct peaks appear at 711.02 eV and 724.7 eV that can be assigned to Fe 2p_{3/2} and Fe 2p_{1/2}, respectively. The binding energy difference between Fe 2p_{3/2} and Fe 2p_{1/2} is about 13.68 eV. In addition, there are distinct satellite (Sat.) peaks at around 719.5 eV and 739.5 eV; the binding energy difference between the satellite peak at around 719.5 eV and that of Fe 2p_{3/2} is 8.48 eV. All the above evidence further demonstrates that FeO_x in $\gamma-Fe_2O_3/nf-MnO_2-ATP$ is in the form of $\gamma-Fe_2O_3$, which is consistent with other literature reports.^{35,36}

As shown in Fig. 4d, two distinct peaks can be separated in the O 1s spectra by performing the same peak-fitting deconvolution technique. The peak at a lower binding energy (529.6 to 530.2 eV) is ascribed to lattice oxygen (marked as O_β); the other peak at a higher binding energy (531.6 to 532.0 eV) is related to chemisorbed oxygen (marked as O_α), which includes O₂²⁻ or O⁻, corresponding to defect oxide or hydroxyl-like groups, respectively.^{37,38} It has been reported that surface-adsorbed oxygen O_α presents higher mobility compared to lattice oxygen O_β, which has more activity in oxidation reactions.³⁹ According to the XPS results of O 1s, the ratios of O_α/(O_α + O_β) in $nf-MnO_2-ATP$ and $\gamma-Fe_2O_3/nf-MnO_2-ATP$ are 55.6% and 61.2%, respectively, which demonstrates that the surface active oxygen O_α components obviously increase after modification with $\gamma-Fe_2O_3$. A high relative concentration ratio of O_α/(O_α + O_β) on the catalyst

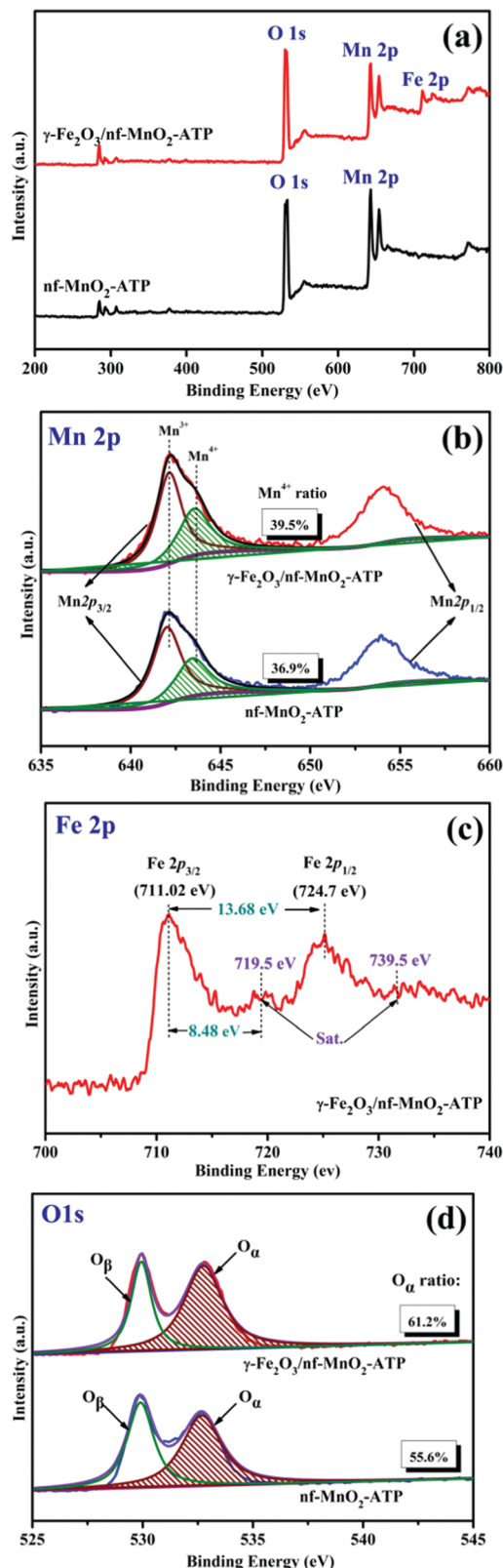


Fig. 4 XPS survey spectra of $\text{nf-MnO}_2\text{-ATP}$ and $\gamma\text{-Fe}_2\text{O}_3/\text{nf-MnO}_2\text{-ATP}$ (a); high-resolution spectra of Mn 2p (b), Fe 2p (c), and O 1s (d).

surface is correlated with high SCR activity. Meanwhile, the presence of more surface adsorbed oxygen on the catalyst

Table 3 Atomic concentrations on the surface of the catalysts determined by XPS

Catalysts	Atomic concentration (at%)			Relative atomic ratio (at%)		
	Mn	Fe	O	Mn^{4+}/Mn	Fe^{3+}/Fe $O_\alpha/(O_\alpha + O_\beta)$	
$\text{nf-MnO}_2\text{-ATP}$	47.78	—	52.22	36.9	—	55.6
$\gamma\text{-Fe}_2\text{O}_3/\text{nf-MnO}_2\text{-ATP}$	34.86	11.6	53.54	39.5	100	61.2

surface is beneficial to oxidation of NO and adsorption of NH_3 . It is generally believed that NH_3 adsorption in the form of NH_4^+ can also be enhanced due to the production of larger amounts of surface hydroxyl groups, which act as Brønsted acid sites. The formed NH_4^+ can react with adsorbed NO_2 to produce active intermediate species and then further react with gaseous NO to produce N_2 and H_2O ,³⁹ thus improving the denitration rate.

$\text{NH}_3\text{-TPD}$ analysis

It is commonly believed that NH_3 molecules can be adsorbed and activated by acid sites on the surfaces of catalysts; this is viewed as a crucial step during the $\text{NH}_3\text{-SCR}$ process. Hence, the $\text{NH}_3\text{-TPD}$ was measured to evaluate the strength distributions and the amounts of acidic sites on the catalyst surfaces. As shown in Fig. 5, both $\text{nf-MnO}_2\text{-ATP}$ and $\gamma\text{-Fe}_2\text{O}_3/\text{nf-MnO}_2\text{-ATP}$ present three distinct desorption peaks. The desorption peaks observed below 200 °C (denoted as α) and the desorption peaks between 300 °C and 400 °C (denoted as β) can be assigned to the NH_3 desorbed by weak acid sites and medium acid sites on the catalysts, respectively.

The peaks above 450 °C (denoted as γ) can be attributed to chemisorbed NH_3 molecules adsorbed by the strong acid sites.⁴⁰ It is generally recognized that NH_4^+ ions coordinated to Brønsted acid sites are less thermally stable than NH_3 molecules bound to Lewis acid sites. The desorption peaks at low temperature (below 350 °C) are associated with coordinated

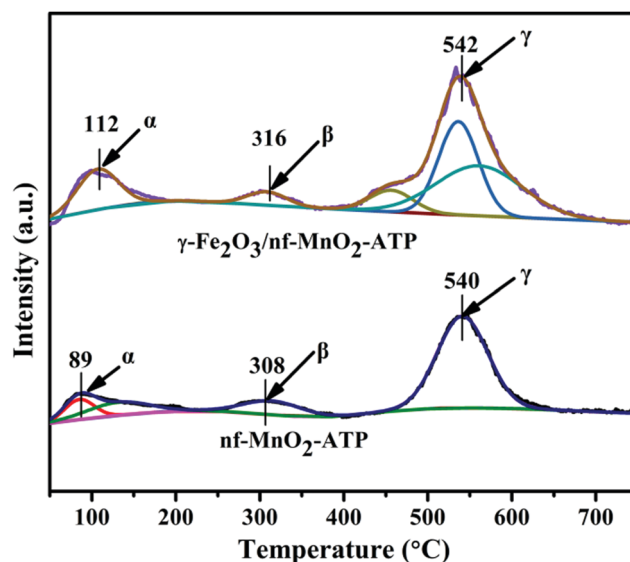


Fig. 5 $\text{NH}_3\text{-TPD}$ profiles of $\text{nf-MnO}_2\text{-ATP}$ and $\gamma\text{-Fe}_2\text{O}_3/\text{nf-MnO}_2\text{-ATP}$.

Table 4 NH₃-TPD peak areas of the catalysts

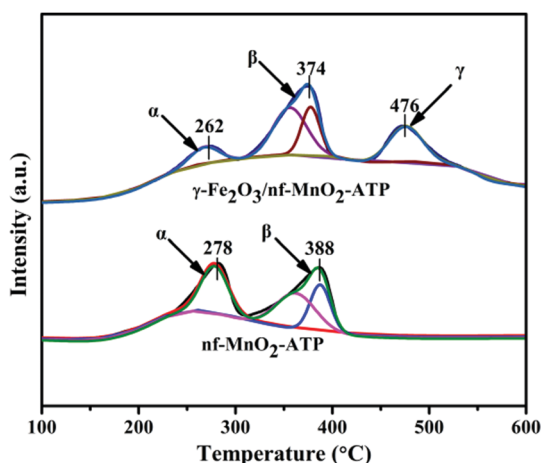
Catalyst	Peak α ($\mu\text{mol g}^{-1}$)	Peak β ($\mu\text{mol g}^{-1}$)	Peak γ ($\mu\text{mol g}^{-1}$)
nf-MnO ₂ -ATP	174.6	65.7	579.2
γ -Fe ₂ O ₃ /nf-MnO ₂ -ATP	205.7	100.8	1119.1

NH₄⁺ ions derived from the Brønsted acid sites, whereas the desorption peaks at high temperature (above 400 °C) are assigned to NH₃ molecules binding to Lewis acid sites.^{41,42} This NH₃ desorption peak of γ -Fe₂O₃/nf-MnO₂-ATP shifts obviously to the high-temperature side, indicating that the surface acidity of the catalyst is significantly enhanced after modification with γ -Fe₂O₃ nanoparticles.⁴³

Moreover, the integral areas of the peaks in nf-MnO₂-ATP and γ -Fe₂O₃/nf-MnO₂-ATP were calculated in order to compare the NH₃ desorption amounts. As shown in Table 4, γ -Fe₂O₃/nf-MnO₂-ATP has a high NH₃ adsorption capacity relative to nf-MnO₂-ATP. Combined with the above analysis, the improvement of the catalyst acid strength and the increase of surface NH₃ adsorption will be beneficial to the NH₃-SCR reaction.

H₂-TPR measurements

H₂-TPR measurements were also performed to investigate the reducibility of the catalysts. In the profile of nf-MnO₂-ATP (Fig. 6), two obvious reduction peaks appeared at 278 °C and 388 °C, respectively. These mainly arise from the gradual reduction of surface manganese oxides. The first peak at 278 °C can be assigned to the reduction peak of MnO₂ to Mn₂O₃, and the second one at 388 °C may be due to reduction of Mn₂O₃ to MnO.^{44,45} In comparison to nf-MnO₂-ATP, there is an evident reduction peak at 476 °C in the γ -Fe₂O₃/nf-MnO₂-ATP profile in addition to peaks at 262 °C and 374 °C. According to the literature,^{19,46} the reduction peak around 380 °C is related to the reduction of γ -Fe₂O₃ to Fe₃O₄ and the other at 510 °C can be attributed to the reduction of Fe₃O₄ to FeO. Therefore, the reduction peak at 476 °C may be attributable to overlapping resulting from the reduction of γ -Fe₂O₃ to Fe₃O₄ and of Fe₃O₄ to FeO.

Fig. 6 H₂-TPR profiles of the catalysts.Table 5 H₂-TPR peak areas of the catalysts

Catalyst	Peak α ($\mu\text{mol g}^{-1}$)	Peak β ($\mu\text{mol g}^{-1}$)	Peak γ ($\mu\text{mol g}^{-1}$)
nf-MnO ₂ -ATP	51.7	94.9	—
γ -Fe ₂ O ₃ /nf-MnO ₂ -ATP	19.5	96.3	48.4

Additionally, the H₂ reduction peak of γ -Fe₂O₃/nf-MnO₂-ATP moves to a lower temperature, showing that γ -Fe₂O₃/nf-MnO₂-ATP has stronger oxidation performance and can oxidize H₂ at low temperatures. A lower reduction temperature is considered to aid the catalytic reaction.^{47,48} Tang *et al.*⁴⁹ studied manganese oxide and found that the strong oxidation performance of MnO₂ mainly arises from Mn⁴⁺. Based on the XPS results, the γ -Fe₂O₃/nf-MnO₂-ATP contains a rich Mn⁴⁺ ratio; this result is consistent with the H₂-TPR results. Usually, the H₂ reduction peak area represents the amount of reduction species on the surface of a catalyst.⁵⁰

Therefore, the area of each reduction peak was estimated by integration, and the results are listed in Table 5. It can be seen from Table 5 that the surface of γ -Fe₂O₃/nf-MnO₂-ATP contains more reducible species. This proves that surface modification with γ -Fe₂O₃ nanoparticles not only decreases the H₂ reduction temperature of nf-MnO₂-ATP, but also increases the amounts of reducible species on the surface of the catalyst, which is conducive to enhance the catalytic reduction of the surface in the process of NH₃-SCR and can improve the low temperature performance of the catalyst.

NH₃-SCR activity

In order to compare the low temperature performance of the catalysts, the NO_x conversion rates of γ -Fe₂O₃, nf-MnO₂-ATP and γ -Fe₂O₃/nf-MnO₂-ATP were investigated at 100 °C to 300 °C, and the results are shown in Fig. 7. It can be seen from Fig. 7a that the catalytic activity of pristine γ -Fe₂O₃ nanoparticles as a catalyst for NH₃-SCR denitration is relatively poor. The NO_x conversion rate presents a slowly rising trend below 150 °C, increases more rapidly above 150 °C, and reaches around 90% at about 230 °C. Comparing the NO_x conversion rates of nf-MnO₂-ATP and γ -Fe₂O₃/nf-MnO₂-ATP, it can be found that the two catalysts have similar increasing tendencies at first. However, after 120 °C, the NO_x conversion rate of γ -Fe₂O₃/nf-MnO₂-ATP is obviously higher than that of nf-MnO₂-ATP; it can reach more than 92% at about 150 °C and does not decline within 300 °C. It is evident that the γ -Fe₂O₃/nf-MnO₂-ATP catalyst has excellent low-temperature denitration ability and a wide activity temperature range.

In addition, the N₂ selectivities of the present catalysts were investigated (Fig. 7b). For nf-MnO₂-ATP, the N₂ selectivity began to decrease at 150 °C; it reached about 60% when the temperature increased to 300 °C. The main reason for this is that non-selective oxidation of NH₃ results in an increase of N₂O byproduct. For γ -Fe₂O₃/nf-MnO₂-ATP, there was no significant decline, and the selectivity remained at around 85% in the whole temperature range; this proves that γ -Fe₂O₃ has excellent N₂ selectivity. Yang *et al.*⁴⁶ studied a Fe-Mn/TiO₂

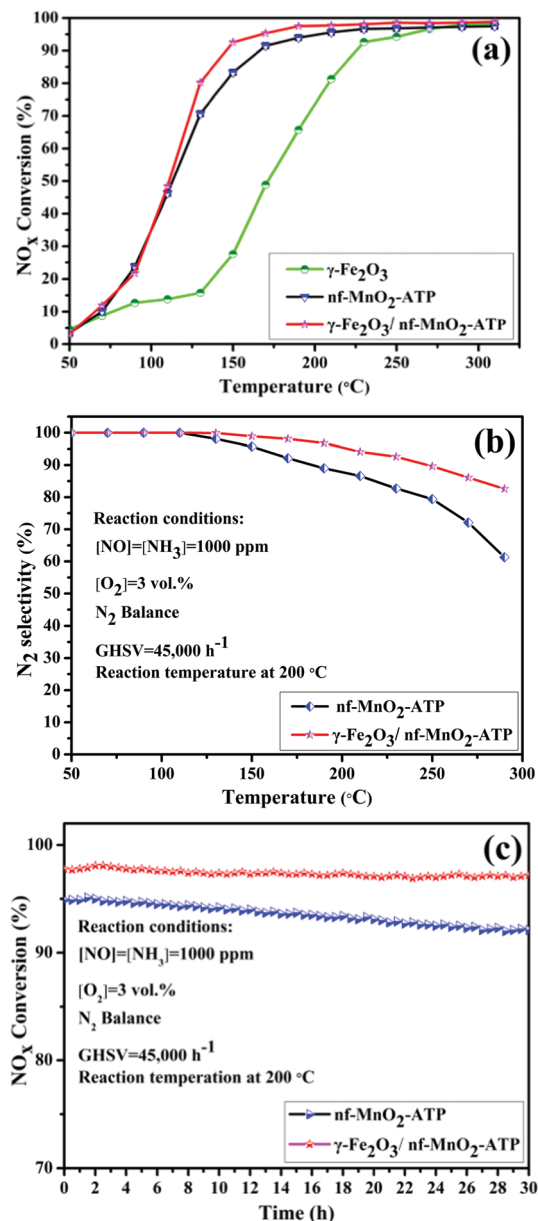


Fig. 7 $\text{NH}_3\text{-SCR}$ performance of $\gamma\text{-Fe}_2\text{O}_3$, $\text{nf-MnO}_2\text{-ATP}$ and $\gamma\text{-Fe}_2\text{O}_3/\text{nf-MnO}_2\text{-ATP}$ (a); N_2 selectivity (b) and stability (c) tests of $\text{nf-MnO}_2\text{-ATP}$ and $\gamma\text{-Fe}_2\text{O}_3/\text{nf-MnO}_2\text{-ATP}$.

denitration catalyst and found that the addition of $\gamma\text{-Fe}_2\text{O}_3$ to the catalyst could decrease the adsorption of Mn^{4+} to NH_3 and thus avoid excessive activation of NH_3 to NH and decreased generation of N_2O . On the basis of this study, it is indicated that surface modification with $\gamma\text{-Fe}_2\text{O}_3$ not only promotes the low-temperature $\text{NH}_3\text{-SCR}$ activity of $\text{nf-MnO}_2\text{-ATP}$, but also increases the N_2 selectivity of the catalyst.

Furthermore, the stabilities of the present catalysts were investigated using 200 °C as the reaction temperature under a mixed atmosphere; the results are shown in Fig. 7c. During a reaction period of 30 h, both the $\text{nf-MnO}_2\text{-ATP}$ and $\gamma\text{-Fe}_2\text{O}_3/\text{nf-MnO}_2\text{-ATP}$ catalysts exhibited better stability. For $\text{nf-MnO}_2\text{-ATP}$, the NO_x conversion rate decreased by about 3%, and for $\gamma\text{-Fe}_2\text{O}_3/\text{nf-MnO}_2\text{-ATP}$,

only about 1% of fluctuation was observed in the whole test process. Zhang *et al.*⁵¹ found that the decreased catalyst stability was mainly due to the aggregation of active group particles on the surface at high temperature and during longtime reaction. In the present work, the active components were coated on the surface of ATP in the form of sheets or nano-flowers. According to the TEM analysis, the modified $\gamma\text{-Fe}_2\text{O}_3$ is mainly adsorbed in the centers of the nano-flakes; with the aid of the physical isolation of the nanopetals, the aggregation phenomenon can be effectively avoided, which can enable the catalyst to retain higher stability in long-time tests.

SO_2 and H_2O resistance tests

In the actual denitration process, flue gas contains small amounts of SO_2 gas and H_2O vapor, and the presence of these substances has a certain effect on $\text{NH}_3\text{-SCR}$ performance. According to reports,⁵² manganese oxide has lower SO_2 resistance ability due to fact that manganese oxide can readily react with SO_2 in flue gas to generate a large amount of sulfate, resulting in a decrease of the amount of the active component of Mn^{4+} and thus leading to a decrease of the catalytic activity. As an excellent denitration material, $\gamma\text{-Fe}_2\text{O}_3$ nanoparticles were modified on the surface of $\text{nf-MnO}_2\text{-ATP}$, which can interact with $\text{nf-MnO}_2\text{-ATP}$ to enhance the ratio of Mn^{4+} on the surface of the catalyst. On the other hand, this can play a protective role and decrease the toxicity of SO_2 gas to $\text{nf-MnO}_2\text{-ATP}$. Therefore, to evaluate the actual application capability of the catalyst, 200 ppm SO_2 was passed during the test process to investigate the $\text{NH}_3\text{-SCR}$ performance changes of the catalyst at 200 °C within 24 h; the results are presented in Fig. 8a. As shown in Fig. 8a, both $\text{nf-MnO}_2\text{-ATP}$ and the $\gamma\text{-Fe}_2\text{O}_3/\text{nf-MnO}_2\text{-ATP}$ maintain high NO_x conversion rates of about 95% and 98%, respectively, in the absence of SO_2 within the first 2 h. Upon the addition of SO_2 to the reaction system, the activities of catalysts show evident declines. After reaction for 5 h, the NO_x conversion rate of $\text{nf-MnO}_2\text{-ATP}$ decreased to *ca.* 59%, and with extension of the test time, the activity continued to slow until it decreased to around 48%; this indicates that the active component on the surface has experienced SO_2 poisoning. After turning off the SO_2 gas, the catalyst activity was gradually restored to *ca.* 55%. Meanwhile, the activity of $\gamma\text{-Fe}_2\text{O}_3/\text{nf-MnO}_2\text{-ATP}$ also decreased after aeration with SO_2 , but it retained better activity of about 89% in the presence of SO_2 compared to $\text{nf-MnO}_2\text{-ATP}$. After stopping SO_2 , the NO_x conversion rate of the catalyst was restored to 94% within 2 h.

In addition, in order to investigate the effects of mixed components on the $\text{NH}_3\text{-SCR}$ activity, 200 ppm SO_2 and 10% H_2O vapor were passed through the reactor (Fig. 8b). After the addition of SO_2 and H_2O vapor, the activity of the catalysts appeared to decrease more significantly than in the presence of SO_2 alone. However, the $\gamma\text{-Fe}_2\text{O}_3/\text{nf-MnO}_2\text{-ATP}$ catalyst retained around 86% NO_x conversion during the whole test process. After stopping the injection of SO_2 and H_2O vapor, the activity of the catalyst could be restored to around 90%. Xiong *et al.*⁵³ found that the effects of H_2O on catalyst activity arise mainly because the presence of H_2O vapor in the system will form

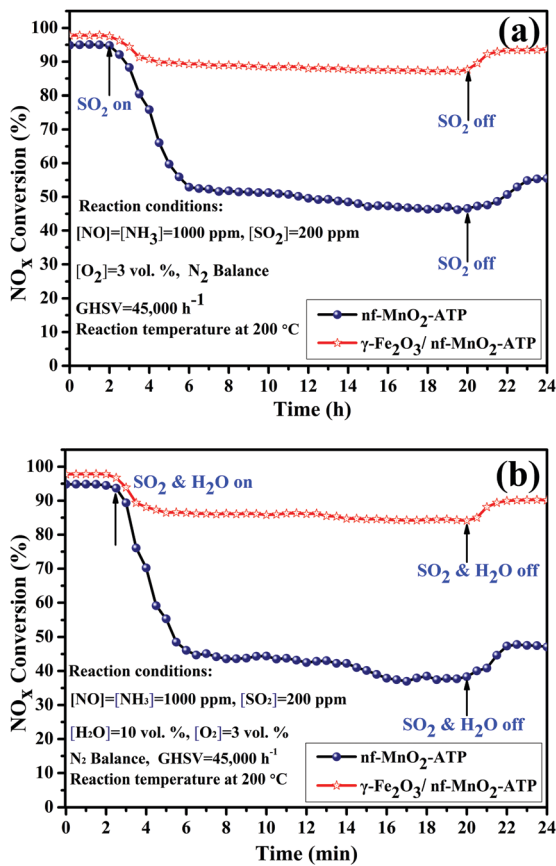


Fig. 8 NO_x conversion over the $\text{nf-MnO}_2\text{-ATP}$ and $\gamma\text{-Fe}_2\text{O}_3/\text{nf-MnO}_2\text{-ATP}$ catalysts in the presence of SO_2 (200 ppm) (a) and SO_2 (200 ppm) + 10% H_2O (200 °C) (b) within 24 h.

competitive adsorption with NH_3 on the surface of the catalyst, resulting in a decrease of the adsorption quantity of NH_3 on the catalyst acidic sites and, thus, a decrease in the activity of the catalyst. On the basis of the above $\text{NH}_3\text{-TPD}$ analysis, the surface acid sites of the catalyst obviously increased after modification with $\gamma\text{-Fe}_2\text{O}_3$, which is more advantageous to the adsorption of NH_3 on the catalyst surface and thus decreases the H_2O poisoning of the catalyst. This excellent performance can enable the catalyst to maintain good denitration performance in the presence of SO_2 and H_2O vapor.

In addition, the effects of H_2O and SO_2 on the catalytic performance were investigated *via* studying the morphology changes of the catalysts. Fig. 9 shows SEM images of the $\gamma\text{-Fe}_2\text{O}_3/\text{nf-MnO}_2\text{-ATP}$ catalyst before and after the H_2O and SO_2 test. It can be observed from Fig. 9a that the active component of the catalyst before the H_2O and SO_2 test is evenly coated on the surface of the ATP, and the flower-like morphology is clearly visible. Meanwhile, the surface of the catalyst after the H_2O and SO_2 test shows abnormal attachments, and the flower-like structures are covered and almost invisible. According to the literature,⁵⁴ these surface attachments are classified as ammonium sulfate species, such as NH_4HSO_4 , $(\text{NH}_4)_2\text{SO}_4$, and NH_4HSO_3 ; these can form surface metal sulphates on the catalyst, thus weakening the metal-oxygen bonds (M-O) in

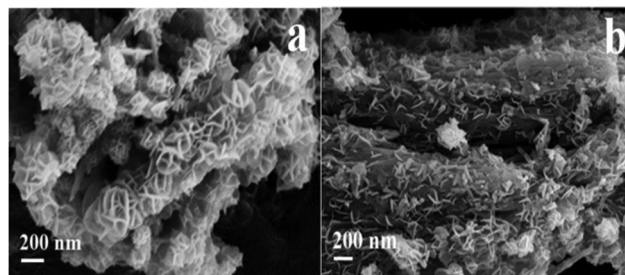


Fig. 9 SEM images of the $\gamma\text{-Fe}_2\text{O}_3/\text{nf-MnO}_2\text{-ATP}$ catalyst before (a) and after (b) the H_2O and SO_2 test.

the catalyst to produce the stretching vibrations of surface sulfates (S-O) and metal sulfates (S=O). This is due to the accumulation of sulphur ammonia species and blockage of the pores, which deactivate the catalyst.^{55,56}

Based on the above results, the mechanism of the enhanced performance of the $\gamma\text{-Fe}_2\text{O}_3/\text{nf-MnO}_2\text{-ATP}$ catalyst can be proposed as follows. First, It is known from the XRD results that the surface Fe and Mn active materials have good crystallinity and Fe mainly exists in the form of $\gamma\text{-Fe}_2\text{O}_3$, which can decrease the adsorption of NH_3 on Mn^{4+} , thus avoiding excessive activation of NH_3 to NH , and can decrease the generation of N_2O ; this indicates that surface modification by $\gamma\text{-Fe}_2\text{O}_3$ can not only promote the low-temperature $\text{NH}_3\text{-SCR}$ activity of $\text{nf-MnO}_2\text{-ATP}$, but can also increase the N_2 selectivity of the catalyst. Second, it is evident from the TEM images that $\gamma\text{-MnO}_2$ is uniformly coated on the surface of ATP with a petal-like morphology, which proves that $\gamma\text{-Fe}_2\text{O}_3/\text{nf-MnO}_2\text{-ATP}$ has an excellent surface morphology that is beneficial for uniform dispersion of $\gamma\text{-Fe}_2\text{O}_3$ and thus avoids catalyst aggregation in practical applications under high temperature conditions. The charge attraction between the components can strengthen the combination of $\gamma\text{-Fe}_2\text{O}_3$ and $\text{nf-MnO}_2\text{-ATP}$, thus decreasing aggregation and shedding of the particles in the test process. Additionally, it is stated that the larger specific surface area and pore volume of $\gamma\text{-Fe}_2\text{O}_3/\text{nf-MnO}_2\text{-ATP}$ illustrated by the BET method are more advantageous to adsorption and contact of gas on the surface, which can provide more reaction sites for catalytic reaction; this will help improve the NO_x conversion rate of the catalyst. In addition, XPS tests show that surface modification with $\gamma\text{-Fe}_2\text{O}_3$ can increase the Mn^{4+} and surface adsorption oxygen O_x contents of $\text{nf-MnO}_2\text{-ATP}$, which favours the oxidation of NH_3 and NO on the catalyst surface. At the same time, the $\text{H}_2\text{-TPR}$ results indicate that $\gamma\text{-Fe}_2\text{O}_3/\text{nf-MnO}_2\text{-ATP}$ is rich in reducing species on the surface of $\text{nf-MnO}_2\text{-ATP}$, which is conducive to the reduction of $\text{NH}_3\text{-SCR}$. It was found by $\text{NH}_3\text{-TPD}$ that $\gamma\text{-Fe}_2\text{O}_3/\text{nf-MnO}_2\text{-ATP}$ has more acidic sites and can adsorb more NH_3 in the $\text{NH}_3\text{-SCR}$ reaction. Therefore, $\gamma\text{-Fe}_2\text{O}_3/\text{nf-MnO}_2\text{-ATP}$ has good denitration performance for low temperature SCR of NO_x with NH_3 .

Conclusions

A $\gamma\text{-Fe}_2\text{O}_3/\text{nf-MnO}_2\text{-ATP}$ catalyst has been fabricated through a facile hydrothermal method. The largest specific area of the

as-prepared $\gamma\text{-Fe}_2\text{O}_3/\text{nf-MnO}_2\text{-ATP}$ was as high as $199.7\text{ m}^2\text{ g}^{-1}$, and the pore volume of $\gamma\text{-Fe}_2\text{O}_3/\text{nf-MnO}_2\text{-ATP}$ also showed a significant increase. It is stated that a larger specific surface area and pore volume are advantageous to adsorption and contact of gas on the surface, which can provide more reaction sites for the catalytic reaction and help improve the NO_x conversion rate of the catalyst. Furthermore, in contrast to $\text{nf-MnO}_2\text{-ATP}$, $\gamma\text{-Fe}_2\text{O}_3/\text{nf-MnO}_2\text{-ATP}$ exhibited a higher NO_x conversion of 92% at about $150\text{ }^\circ\text{C}$, superior N_2 selectivity, and better SO_2 and H_2O resistance, as well as good stability. Therefore, the as-prepared $\gamma\text{-Fe}_2\text{O}_3/\text{nf-MnO}_2\text{-ATP}$ catalyst has potential alternative applications in $\text{NH}_3\text{-SCR}$ with a broad operation temperature range.

Conflicts of interest

There are no conflicts to declare.

Acknowledgements

This work was supported by the Social Development Fund of Jiangsu Province (No. BE2016654, CE20165022) and the Advance Catalysis and Green Manufacturing Collaborative Innovation Center, Changzhou University (TAPP No. PPZY2015B145).

Notes and references

- C. J. Tang, H. L. Zhang and L. Dong, *Catal. Sci. Technol.*, 2016, **6**, 1248–1264.
- F. D. Liu, Y. B. Yu and H. He, *Chem. Commun.*, 2014, **50**, 8445–8463.
- Q. C. Liu, S. F. Chen, Z. Y. Li and Q. Y. Liu, *Appl. Catal., B*, 2015, **164**, 475–482.
- F. Tang, B. L. Xu, H. H. Shi, J. H. Qiu and Y. N. Fan, *Appl. Catal., B*, 2010, **94**, 71–76.
- O. Kroecher and M. Elsener, *Appl. Catal., B*, 2008, **77**, 215–227.
- P. R. Ettireddy, N. Ettireddy, S. Mamedov, P. Boolch and P. G. Smirniotis, *Appl. Catal., B*, 2007, **76**, 123–134.
- S. G. Zhang, B. L. Zhang, B. Liu and S. L. Sun, *RSC Adv.*, 2017, **7**, 26226–26242.
- X. B. Wang, S. G. Wu, W. X. Zou, S. H. Yu, K. T. Gui and L. Dong, *Chin. J. Catal.*, 2016, **37**, 1314–1323.
- C. L. Li, X. L. Tang, H. H. Yia, L. F. Wang, X. X. Cui, C. Chu, J. Y. Li, R. C. Zhang and Q. J. Yu, *Appl. Surf. Sci.*, 2018, **428**, 924–932.
- A. J. Xie, X. M. Zou, X. Y. Huang, L. Ji, W. T. Zhou, S. P. Luo and C. Yao, *J. Ind. Eng. Chem.*, 2017, **49**, 230–241.
- L. J. Yan, Y. Y. Liu, K. W. Zha, H. R. Li, L. Y. Shi and D. S. Zhang, *ACS Appl. Mater. Interfaces*, 2017, **9**, 2581–2593.
- Z. H. Chen, X. H. Li, X. Gao, Y. B. Jiang, Y. X. Lv, F. R. Wang and L. F. Wang, *Chin. J. Catal.*, 2009, **30**, 4–6.
- D. Fang, J. L. Xie, H. Hu, Y. H. Yang, F. He and Z. B. Fu, *Chem. Eng. J.*, 2015, **271**, 23–30.
- R. M. Liu, Y. W. Jiang, Q. Chen, Q. Y. Lu, W. Du and F. Gao, *RSC Adv.*, 2013, **3**, 8261–8268.
- L. J. France, Q. Yang, W. Li, Z. H. Chen, J. Y. Guang, D. W. Guo, L. F. Wang and X. H. Li, *Appl. Catal., B*, 2017, **206**, 203–215.
- C. X. Liu, S. J. Yang, L. Ma, Y. Peng, A. Hamidreza, H. Z. Chang and J. Li, *Catal. Lett.*, 2013, **143**, 697–704.
- K. W. Zha, L. Kang, C. Feng, L. P. Han, H. R. Li, T. T. Yan, P. Maitarad, L. Y. Shi and D. S. Zhang, *Environ. Sci.: Nano*, 2018, **5**, 1408–1419.
- K. W. Zha, S. X. Cai, H. Hu, H. R. Li, T. T. Yan, L. Y. Shi and D. S. Zhang, *J. Phys. Chem. C*, 2017, **121**, 25243–25254.
- X. M. Zhou, X. Y. Huang, A. J. Xie, S. P. Luo, C. Yao, X. Z. Li and S. X. Zuo, *Chem. Eng. J.*, 2017, **326**, 1074–1085.
- S. P. Luo, W. T. Zhou, A. J. Xie, F. Q. Wu, C. Yao, X. Z. Li, X. S. Zuo and T. H. Liu, *Chem. Eng. J.*, 2016, **286**, 291–299.
- J. S. Zhang, T. J. Yao, H. Zhang, X. Zhang and J. Wu, *Nanoscale*, 2016, **8**, 18693–18702.
- H. Xia, M. O. Lai and L. Li, *J. Mater. Chem.*, 2010, **20**, 6896–6902.
- Z. J. Dai, X. W. Yu, C. Huang, M. Li, J. F. Su, Y. P. Guo, H. Xu and Q. F. Ke, *RSC Adv.*, 2016, **6**, 97022–97029.
- M. S. P. Shaffer, X. Fan and A. H. Windle, *Carbon*, 1998, **36**, 1603–1612.
- C. C. Wan and J. Li, *ACS Sustainable Chem. Eng.*, 2015, **3**, 2142–2152.
- L. Stagi, J. A. De Toro, A. Ardu, C. Cannas, A. Casu, S. S. Lee and P. C. Ricci, *J. Phys. Chem. C*, 2014, **118**, 2857–2866.
- J. Y. Zhou, H. Zhao, X. M. Mu, J. Y. Chen, P. Zhang, Y. L. Wang, Y. M. He, Z. X. Zhang, X. J. Pan and E. Q. Xie, *Nanoscale*, 2015, **7**, 14697–14706.
- J. Han, D. S. Zhang, P. Maitarad, L. Y. Shi, S. X. Cai, H. R. Li, L. Huang and J. P. Zhang, *Catal. Sci. Technol.*, 2015, **5**, 438–446.
- D. U. Lee, B. J. Kim and Z. W. Chen, *J. Mater. Chem. A*, 2013, **1**, 4754–4762.
- J. Tang, B. Mu, L. Zong, M. S. Zheng and A. Q. Wang, *RSC Adv.*, 2015, **5**, 38443–38451.
- Y. H. Wang, M. Q. Chen, Z. L. Yang, T. Liang, S. M. Liu, Z. S. Zhou and X. J. Li, *Appl. Catal., A*, 2018, **550**, 214–227.
- W. Li, R. T. Guo, S. X. Wang, W. G. Pan, Q. L. Chen, M. Y. Li, P. Sun and S. M. Liu, *Fuel Process. Technol.*, 2016, **154**, 235–242.
- H. Hu, S. X. Cai, H. R. Li, L. Huang, L. Y. Shi and D. S. Zhang, *ACS Catal.*, 2015, **5**, 6069–6077.
- T. Wang, Z. T. Wan, X. C. Yang, X. Y. Zhang, X. X. Niu and B. M. Sun, *Fuel Process. Technol.*, 2018, **169**, 112–121.
- M. Kaloti and A. Kumar, *J. Phys. Chem. C*, 2016, **120**, 17627–17644.
- X. L. Cui, Q. L. Zhang, M. Tian and Z. P. Dong, *New J. Chem.*, 2017, **41**, 10165–10173.
- P. Sun, R. T. Guo, S. M. Liu, S. X. Wang, W. G. Pan and M. Y. Li, *Appl. Catal., A*, 2017, **531**, 129–138.
- W. P. Shan, F. D. Liu, H. He, X. Y. Shi and C. B. Zhang, *Appl. Catal., B*, 2012, **115**, 100–106.
- F. D. Liu, H. He, Y. Ding and C. B. Zhang, *Appl. Catal., B*, 2009, **93**, 194–204.

- 40 C. Fang, D. S. Zhang, L. Y. Shi, R. H. Gao, H. G. Li, L. P. Ye and J. P. Zhang, *Catal. Sci. Technol.*, 2013, **3**, 803–811.
- 41 Y. Li, Y. P. Li, P. F. Wang, W. P. Hu, S. G. Zhang, Q. Shi and S. H. Zhan, *Chem. Eng. J.*, 2017, **330**, 213–222.
- 42 J. Shi, Z. Z. Zhang, M. G. Chen, Z. X. Zhang and W. F. Shangguan, *Fuel*, 2017, **210**, 783–789.
- 43 L. Zhang, L. Y. Shi, L. Huang, J. P. Zhang, R. H. Gao and D. S. Zhang, *ACS Catal.*, 2014, **4**, 1753–1763.
- 44 S. S. R. Putluru, L. Schill, A. D. Jensen, B. Siret, F. Tabaries and R. Fehrmann, *Appl. Catal., B*, 2015, **165**, 628–635.
- 45 P. Lu, H. Li, H. Y. Liu, Y. F. Chen and Z. K. Zhang, *RSC Adv.*, 2017, **7**, 19771–19779.
- 46 S. J. Yang, C. X. Liu, H. Z. Chang, L. Ma, Z. Qu, N. Q. Yan, C. Z. Wang and J. H. Li, *Ind. Eng. Chem. Res.*, 2013, **52**, 5601–5610.
- 47 R. H. Gao, D. S. Zhang, P. Maitarad, L. Y. Shi, T. Rungrotmongkol, H. R. Li, J. P. Zhang and W. G. Cao, *J. Phys. Chem. C*, 2013, **117**, 10502–10511.
- 48 C. Z. Shao, X. F. Liu, D. M. Meng, Q. Xu, Y. L. Guo, Y. Guo, W. C. Zhan, L. Wang and G. Z. Luo, *RSC Adv.*, 2016, **6**, 66169–66179.
- 49 X. F. Tang, J. H. Li, L. Sun and J. M. Hao, *Appl. Catal., B*, 2010, **99**, 156–162.
- 50 S. X. Cai, D. S. Zhang, L. Y. Shi, J. Xu, L. Zhang, L. Huang, H. R. Li and J. P. Zhang, *Nanoscale*, 2014, **6**, 7346–7353.
- 51 L. Zhang, D. S. Zhang, J. P. Zhang, S. X. Cai, C. Fang, L. Huang, H. R. Li, R. H. Gao and L. Y. Shi, *Nanoscale*, 2013, **5**, 9821–9829.
- 52 W. Q. Xu, H. He and Y. B. Yu, *J. Phys. Chem. C*, 2009, **113**, 4426–4432.
- 53 S. C. Xiong, Y. Liao, X. Xiao, H. Dang and S. J. Yang, *Catal. Sci. Technol.*, 2015, **5**, 2132–2140.
- 54 F. Gao, X. Tang, H. Yi, S. Z. Zhao, J. G. Wang and T. Gu, *Appl. Surf. Sci.*, 2019, **466**, 411–424.
- 55 H. Abdulhamid, E. Fridell, J. Dawody and M. Skoglundh, *J. Catal.*, 2006, **241**, 200–210.
- 56 T. Yamaguchi, T. Jin and K. Tanabe, *J. Phys. Chem.*, 1986, **90**, 3148–3152.